

RESEARCH ARTICLE

View Article Online
View Journal | View Issue

Cite this: *Mater. Chem. Front.*,
2020, 4, 996

Facile synthesis of nickel–copper hollow spheres as efficient bifunctional electrocatalysts for overall water splitting†

Lifeng Lin, Min Chen and Limin Wu *

Received 13th November 2019,
Accepted 25th January 2020

DOI: 10.1039/c9qm00697d

rsc.li/frontiers-materials

Sustainable energy conversion has motivated researchers to design and develop novel efficient bifunctional electrocatalysts for water splitting. In this work, we report the facile synthesis of $\text{Ni}_x\text{Cu}_y\text{@C}$ hollow spheres by using a template-free strategy. The activities of the hydrogen evolution reaction (HER) and the oxygen evolution reaction (OER) are significantly enhanced by the hollow structure and optimal composition. The as-synthesized $\text{Ni}_4\text{Cu}_2\text{@C}$ hollow spheres exhibit superior HER performance with overpotentials of 55 and 91 mV at 10 mA cm^{-2} in alkaline and acidic media, and the low overpotential of 280 mV at 10 mA cm^{-2} for the OER in alkaline media. When $\text{Ni}_4\text{Cu}_2\text{@C}$ hollow spheres are employed as electrocatalysts for both the anode and cathode in an overall water splitting system, a cell voltage of only 1.49 V at 15 mA cm^{-2} and long-term durability (50 h@ 40 mA cm^{-2}) are achieved.

Introduction

Hydrogen (H_2) possesses high gravimetric energy density and energy conversion efficiency, and is known as an ideal and promising sustainable energy candidate to replace fossil fuels.^{1–4} Electrochemical water splitting is an efficient method of hydrogen production, which consists of two half reactions, including the hydrogen evolution reaction (HER) on the cathode and the oxygen evolution reaction (OER) on the anode. While platinum group metals (PGMs) such as Pt-, Ir-, and Ru-based materials are considered to be the state-of-the-art catalysts for the HER and the OER because of their high catalytic efficiency, their high cost and rareness severely hinder their wide application in water-splitting systems.^{5–8}

To address this issue, much effort has been made to develop earth-abundant, economic alternatives for efficient electrolytic water splitting,^{9–12} and in particular the alloys and compounds containing first-row transition metals (e.g. Ni, Fe, and Co) have attracted tremendous interest owing to their earth abundance and remarkable HER and OER performances.^{13–18} Nonetheless, the HER and OER performances of most Ni-based electrocatalysts are not comparable with that of the Pt/Ir or Pt/RuO₂ couple, thus limiting their practical applications in water electrolysis.^{19–21}

Recently, a number of hollow structure Ni-based nanomaterials, including nanochains,²² nanocages,²³ nanospheres,²⁴ etc., have been synthesized to exhibit enhanced performance of energy conversion devices because the nanostructure can maximize the accessible active sites with a large surface area and a short diffusion path.^{25–28} However, the synthetic processes based on hard-template and soft-template methods seem to be tedious and difficult to control.^{29–33}

Herein, we report a novel bimetallic $\text{Ni}_x\text{Cu}_y\text{@C}$ hollow sphere derived from the Ni_xCu_y -glycerate ($\text{Ni}_x\text{Cu}_y\text{-G}$) hollow spheres fabricated *via* a facile template-free solvothermal method. Owing to the optimal composition and prominent structure, the as-obtained $\text{Ni}_4\text{Cu}_2\text{@C}$ hollow spheres present outstanding HER electrocatalytic activity with overpotentials of 55 and 91 mV at 10 mA cm^{-2} in alkaline and acidic media, and a low overpotential of 280 mV at 10 mA cm^{-2} for the OER in alkaline media. When $\text{Ni}_4\text{Cu}_2\text{@C}$ hollow spheres are employed as electrocatalysts for both the anode and the cathode in an overall water splitting system, a cell voltage of only 1.49 V at 15 mA cm^{-2} and long-term durability (50 h@ 40 mA cm^{-2}) can be achieved. These electrocatalytic properties are considerably better than most of the previously reported Ni-based electrocatalysts, making the $\text{Ni}_4\text{Cu}_2\text{@C}$ hollow spheres versatile electrodes for highly efficient overall water splitting.

Experimental section

Chemicals and materials

$\text{Ni}(\text{NO}_3)_2 \cdot 6\text{H}_2\text{O}$, $\text{Cu}(\text{NO}_3)_2 \cdot 3\text{H}_2\text{O}$, glycerol, isopropanol, 5 wt% Nafion solution and carbon paper were purchased from Sinopharm

Department of Materials Science and State Key Laboratory of Molecular Engineering of Polymers, Fudan University, Shanghai 20043, China.

E-mail: lmw@fudan.edu.cn

† Electronic supplementary information (ESI) available: Characterization data (TEM, SEM, Raman spectra, XRD, XPS, electrochemical measurement tests, and so forth) and comparison of the catalytic activity of various bifunctional electrocatalysts. See DOI: 10.1039/c9qm00697d

Chemical Reagent Co., Ltd. 20 wt% Pt/C and Ir/C were purchased from Premetek Co.

Synthesis of Ni_xCu_y@C hollow spheres

Typically, 0.25 mmol of Ni(NO₃)₂·6H₂O, 0.125 mmol of Cu(NO₃)₂·3H₂O and 8 mL of glycerol were dissolved into 40 mL of isopropanol to form a transparent solution, which was then transferred to a Teflon-lined stainless steel autoclave and kept at 180 °C for 6 h. After being cooled to room temperature naturally, the precipitate was separated by centrifugation, washed several times with ethanol and dried in an oven at 60 °C. A series of Ni_xCu_y-G hollow spheres with different scales of cavities was obtained with different molar ratios of Ni(NO₃)₂·6H₂O and Cu(NO₃)₂·3H₂O. The as-prepared Ni_xCu_y-G precursors were placed in a tube furnace and heated at 500 °C for 1 h at a heating rate of 2 °C min⁻¹ under a H₂/Ar (5:95) atmosphere to obtain Ni_xCu_y@C hollow spheres.

Characterization

The structures and morphologies were obtained *via* transmission electron microscopy (TEM) (FEI, Tecnai G² 20 TWIN, 200 kV) and scanning electronic microscopy (SEM) (Zeiss, Ultra 55, 15 kV). The high-angle annular dark field-scanning transmission microscopy (HAADF-STEM) and energy dispersive spectrometry (EDS) were carried out on a JEOL, JEM-2100F. The crystallographic information was recorded by powder X-ray diffraction (XRD) (Bruker, D8 Advance diffractometer with Cu K α radiation λ = 1.5406 Å). The parameters of XRD tests are listed: angular range = 10–80°, step size = 0.02°, and time per step = 0.2 s. Inductively coupled plasma-optical emission spectroscopy (ICP-OES) (Thermo Scientific, iCAP 7400) was used to determine the Ni and Cu contents of the samples. X-ray photoelectron spectroscopy (XPS) was performed on a scanning X-ray microprobe (ULVAC-PHI, PHI 5000C & PHI 5300), using C 1s (284.8 eV) as a reference. The nitrogen adsorption-desorption experiments were operated on a Micromeritics ASAP 2020 system at 77 K. A laser of 532 nm wavelength was used to measure the Raman spectroscopy spectrum (Renishaw, RM 2000).

Electrochemical measurements

All electrochemical measurements were performed on a CHI 760E electrochemistry workstation (CH Instruments) at ambient temperature. The HER and OER catalytic activities were tested in a standard three-electrode system in 1 M KOH (pH 14) and 0.5 M H₂SO₄ (pH 0). A glassy carbon electrode (GCE) (area of 0.196 cm²), a saturated calomel electrode (SCE, in saturated KCl solution) and a graphite rod were used as the working electrode, reference and counter electrode, respectively. The catalyst ink was prepared by dispersing 3 mg of catalyst in 880 μ L of ethanol and 120 μ L of 5 wt% Nafion solution followed by ultrasonication for at least 30 min. Then, a certain volume of the catalyst ink was dropped on the glassy carbon electrode to reach the catalyst loading of 0.2 mg cm⁻². The HER performance was evaluated in H₂-saturated solution and the OER was in O₂-saturated solution. All potentials were converted *versus* a

reversible hydrogen electrode (RHE): $E(\text{vs. RHE}) = E(\text{vs. SCE}) + (0.242 + 0.059 \text{ pH}) \text{ V}$. Prior to all the linear sweep voltammetry (LSV) experiments, a resistance test was applied to compensate the Ohmic potential drop. The level of iR compensation is 90%. LSV was performed at a scan rate of 5 mV s⁻¹ to obtain the polarization curves. Electrochemical impedance spectroscopy (EIS) measurements were performed with a frequency range from 0.1 to 100 000 Hz.

The values of turnover frequency (TOF) can be calculated assuming that all Ni and Cu ions in the catalysts are active and contributed to the catalytic reaction, since the exact number of active sites is not known (the lowest TOF values)

$$\text{TOF} = jS/(\alpha F n)$$

here, j (A cm⁻²) is the measured current density at certain overpotential; S (GCE area, 0.196 cm²) is the surface area of the GCE; α is the number of electrons transferring in the HER or OER; F is the Faraday constant (96485.3 C mol⁻¹), and n is the metal ion molar number (both Ni and Cu) calculated from the ICP results of the as-prepared catalysts (Table S1, ESI[†]). Herein, the TOF was undervalued when all metal atoms were used to calculate it.³⁴

The faradaic efficiency was calculated by the equation

$$\text{Faradic efficiency} = nFm/Q$$

here, n = 2 and 4 for the HER and the OER respectively, F is the Faraday constant (96485.3 C mol⁻¹), m is moles of gas evolved, and Q (C) is the total amount of charge passed through the cell.

Overall water splitting tests were performed in a two-electrode system with the Ni₄Cu₂@C drop casted on pre-treated carbon paper as both the cathode and the anode in 1 M KOH. Before being used, carbon paper was cleaned by diluted HNO₃, deionized water, and acetone with ultrasonication for 5 min in each step. Then the carbon paper was immersed in concentrated H₂SO₄ for 1 h, followed by washing with deionized water and drying at 60 °C overnight. The mass loading was 1.5 mg cm⁻². For the benchmark noble metal-based catalysts, Ir/C/CP(+)||Pt/C/CP(–) was adopted.

Results and discussion

Uniform Ni_xCu_y-G hollow spheres are synthesized *via* a facile one-pot solvothermal method. Fig. 1 shows the typical formation of Ni_xCu_y-G hollow spheres *via* transmission electron microscopy (TEM) and energy dispersive spectrometry (EDS). At stage I, uniform and spherical solid spheres are obtained. A compositional line profile shows that the amount of Cu in the internal domain is greater than Ni. The distributional difference of Ni and Cu can be ascribed to the faster nucleation rate of Cu with glycerol.^{35–37} Therefore, slower nucleation of Ni with glycerol results in the higher content of Ni on the outer side. By extending the reaction time, the cavity can be observed at stage II. The formation of the cavity can be attributed to the diffusion rate difference ($J_{\text{Cu}} - J_{\text{Ni}}$) between Cu and Ni.

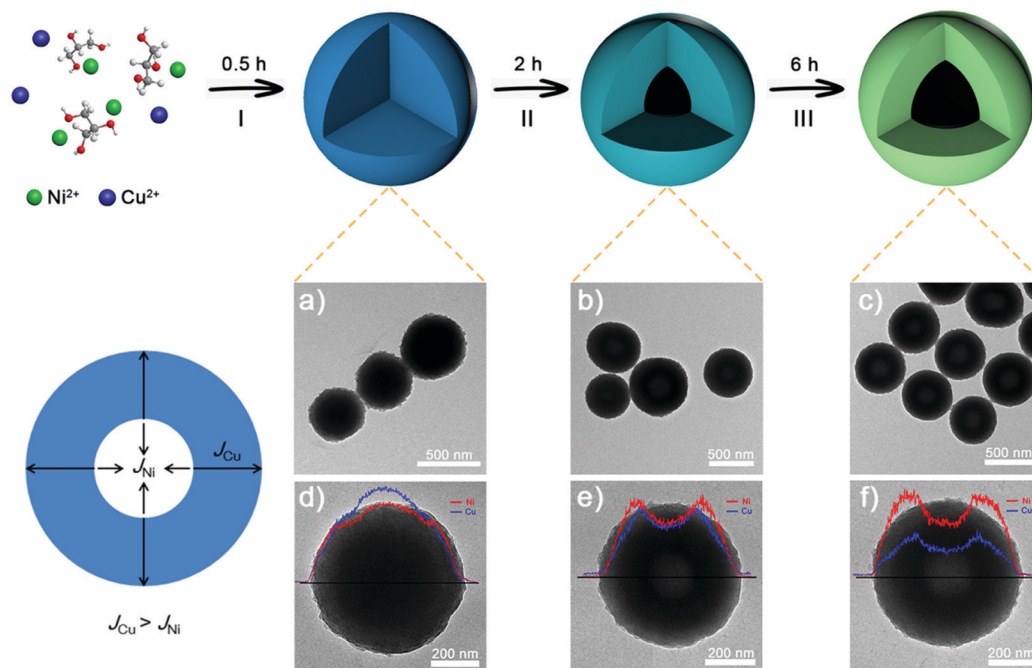


Fig. 1 Schematic illustration of the formation process of $\text{Ni}_x\text{Cu}_y\text{-G}$ hollow spheres.

Under solvothermal conditions, considering the difference of elemental distribution, the outward diffusion of Cu species is faster than the inward diffusion of Ni species in the nanospheres, thus generating internal voids.^{38–40} On the completion of the reaction, the $\text{Ni}_x\text{Cu}_y\text{-G}$ spheres with enlarged hollow interiors are obtained at the end of stage III. Elemental mapping images distinctly show the homogeneous distribution of Ni, Cu, C and O on $\text{Ni}_4\text{Cu}_2\text{-G}$ (Fig. S1, ESI[†]).

Apart from the duration time at 180 °C, another crucial factor in the formation of hollow spheres is the Ni/Cu molar ratio. As shown in Fig. 2, solid spheres are obtained without the addition of Cu. At 4/1 for the Ni/Cu ratio, a small cavity can be seen. The hollow interior becomes bigger with more Cu content. The $\text{Ni}_4\text{Cu}_3\text{-G}$ presents more obvious hollow structures. This is

because higher Cu content has much faster diffusion rate, thus resulting in greater internal voids.

The $\text{Ni}_x\text{Cu}_y\text{-G}$ precursors could be converted into highly crystalline Ni_xCu_y alloys after annealing in a reducing atmosphere. Fig. 3 presents the evolution of the nanostructure along with the decreasing molar ratio of Ni/Cu. Compared to the $\text{Ni}_x\text{Cu}_y\text{-G}$ precursors, the $\text{Ni}_x\text{Cu}_y\text{@C}$ samples reveal spherical structures with more unambiguous cavities. Based on the results of N_2 sorption isotherms (Fig. S2, ESI[†]), the surface specific area of the Ni@C is smallest because of the solid structure. With the higher Cu content, the bigger cavity results in a larger specific area.

The XRD patterns demonstrate that the $\text{Ni}_x\text{Cu}_y\text{@C}$ can be indexed to Ni (JCPDS No. 65-0380) (Fig. 4a). No additional peaks

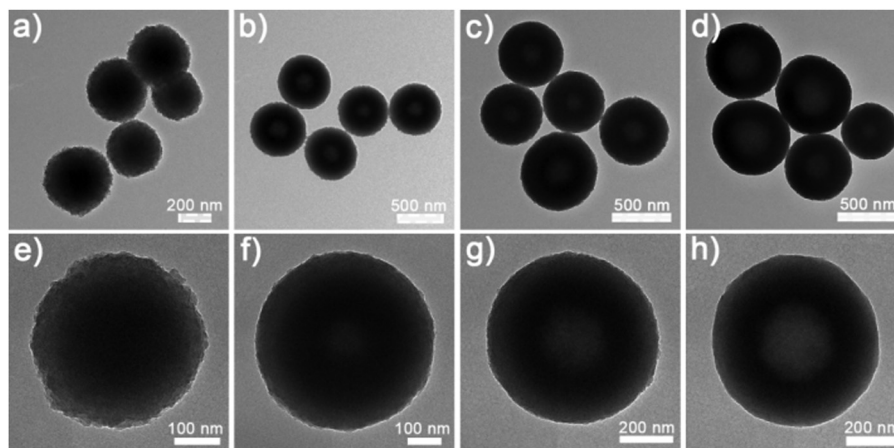


Fig. 2 TEM images of (a and e) Ni-G, (b and f) $\text{Ni}_4\text{Cu}_1\text{-G}$, (c and g) $\text{Ni}_4\text{Cu}_2\text{-G}$ and (d and h) $\text{Ni}_4\text{Cu}_3\text{-G}$.

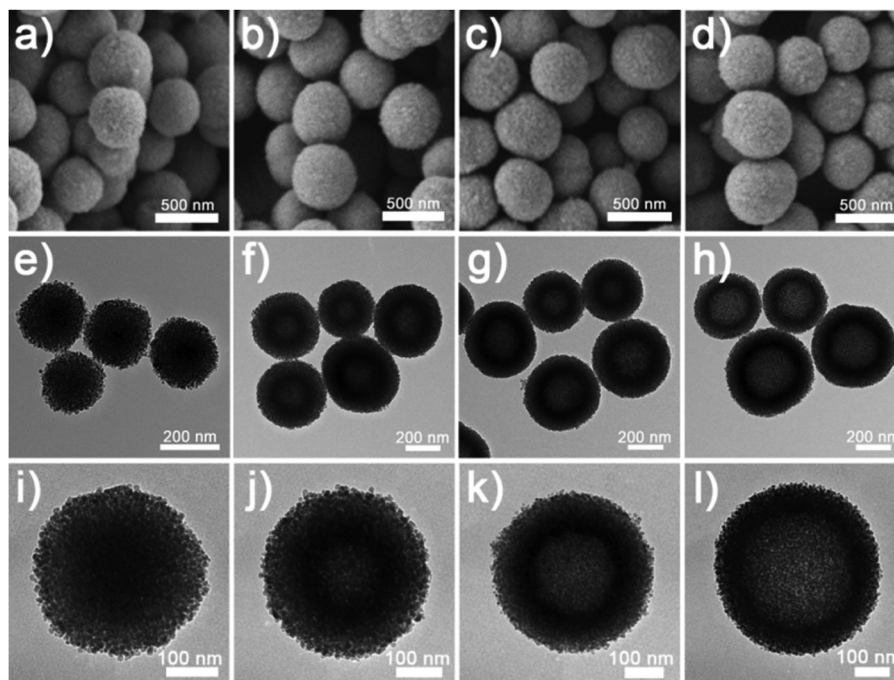


Fig. 3 SEM and TEM images of (a, e and i) Ni@C, (b, f and j) Ni₄Cu₁@C, (c, g and k) Ni₄Cu₂@C and (d, h and l) Ni₄Cu₃@C.

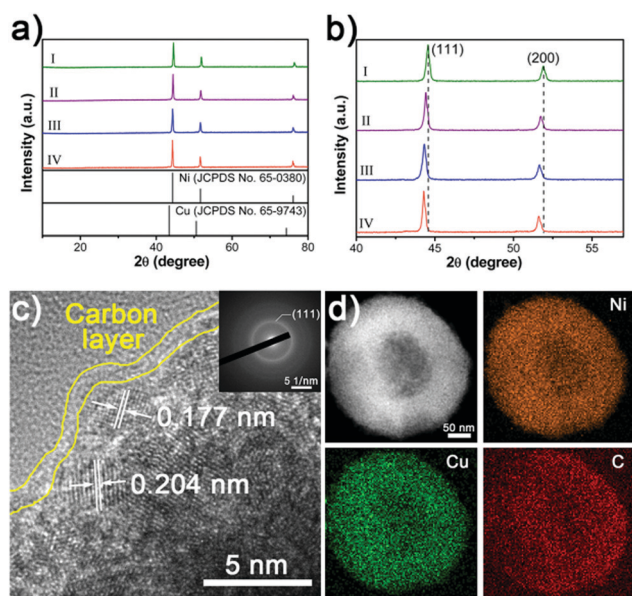


Fig. 4 (a) Typical XRD patterns of Ni_xCu_y@C with different Ni/Cu molar ratios of (I) Ni@C, (II) Ni₄Cu₁@C, (III) Ni₄Cu₂@C, and (IV) Ni₄Cu₃@C; (b) the corresponding zoomed-in regions showing evolution with Cu-incorporation; (c) high-resolution TEM image and SAED (inset) of Ni₄Cu₂@C and (d) HAADF-STEM and the corresponding elemental mapping images of Ni₄Cu₂@C.

can be observed after the incorporation of copper, indicating the pure phase of the crystal structure. However, the peaks (111) and (200) shift to the lower angle by increasing the amount of Cu in Ni_xCu_y@C, suggesting that Cu is indeed incorporated into Ni to form a Ni_xCu_y alloy.^{41,42} In addition,

XPS analysis (Fig. S3a, ESI[†]) indicates that the Ni 2p_{3/2} region displays two dominant peaks of Ni⁰ and Ni–O in which the Ni–O species is ascribed to the inevitable surface oxidation exposed in the air.^{43–45} The high-resolution Cu 2p_{3/2} spectra can be deconvoluted into two major peaks centered at 932.6 and 934.5 eV, as shown in Fig. S3b (ESI[†]), corresponding to Cu⁰ and Cu–O species.^{46,47} Taking Ni₄Cu₂@C hollow spheres as an example, the high-resolution TEM (HRTEM) presents the lattice fringes of 0.204 and 0.177 nm (Fig. 4c), which can be assigned to the interplane spacing of the (111) and (200) planes of nickel.^{41,48,49} The diffusing concentric rings in the selected area electron diffraction (SAED) patterns indicate the polycrystalline structure (Fig. 4c inset). The diffraction rings can be indexed to Ni, in agreement with the XRD analysis. The HAADF-STEM image and the corresponding elemental mapping distinctly show the homogeneous distribution of Ni, Cu, and C (Fig. 4d), indicating uniform doping of Cu into Ni. Raman spectra reveal two characteristic peaks at about 1350 and 1590 cm^{−1} (Fig. S4, ESI[†]), corresponding to D and G bands of graphitic carbon, indicating that the nanoparticles are covered with graphitic carbon.^{50–52} Graphitic carbon encapsulating on the surfaces can impart the NiCu-alloys with fast electron transfer ability to enhance electrocatalytic activity and to protect from etching during the water splitting tests.^{51,53,54}

To investigate the HER performance in basic electrolyte, the as-prepared Ni@C and Ni_xCu_y@C hollow spheres were loaded on the GCE in a standard three-electrode system. Fig. 5a displays the polarization curves with iR compensation obtained in 1 M KOH, with the commercial 20 wt% Pt/C catalyst for comparison. With the overpotential at the current density of 10 mA cm^{−2} (η_{10}) as an indicator, the electrocatalytic performances

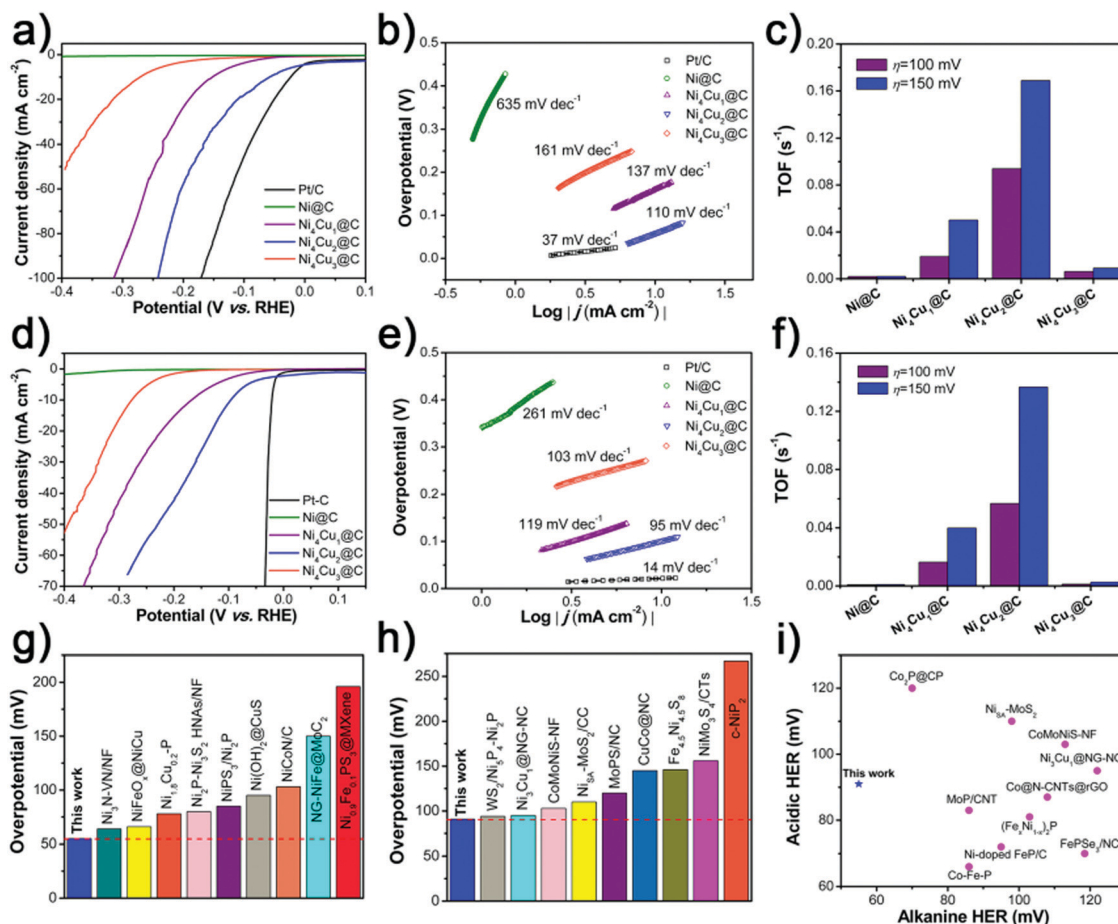


Fig. 5 HER polarization curves, the corresponding Tafel plots and TOFs obtained in (a–c) 1 M KOH, and (d–f) 0.5 M H₂SO₄. Comparison of the overpotential required at 10 mA cm⁻² with other recently reported HER electrocatalysts obtained in (g) 1 M KOH, (h) 0.5 M H₂SO₄ and (i) both acidic and alkaline electrolytes.

vary with the molar ratios of Ni/Cu in Ni_xCu_y@C. The original Ni@C doesn't display any catalytic activity for the HER in basic electrolyte. Incorporating a small amount of Cu can lead to improved performance such as Ni₄Cu₁@C. Furthermore, increasing the Cu addition reveals much better HER catalytic activity, *e.g.*, for Ni₄Cu₂@C with as low as 55 mV overpotential to achieve a current density of 10 mA cm⁻², which is better than those of Ni₄Cu₁@C (152 mV) and Ni₄Cu₃@C catalysts (271 mV). Although 55 mV overpotential for Ni₄Cu₂@C is still not comparable to commercial Pt/C, it has outperformed most of the state-of-art HER electrocatalysts in 1 M KOH (Fig. 5g and Table S2, ESI†). The Tafel plot (η versus $\log j$, η is the overpotential and j represents the current density) of Ni₄Cu₂@C is fitted to be 110 mV dec⁻¹, which is smaller than those of Ni@C (635 mV dec⁻¹), Ni₄Cu₁@C (137 mV dec⁻¹), and Ni₄Cu₃@C (161 mV dec⁻¹), further confirming its rapid HER reaction electrocatalytic kinetics. The turnover frequency (TOF) is another activity metric to gain insight into the intrinsic activity,^{23,55,56} which can be calculated by assuming that all the metal sites (both Ni and Cu) in the catalysts are active. The Ni₄Cu₂@C has a TOF as high as 0.094 s⁻¹, at an overpotential of 100 mV (Fig. 5c), which is much higher than those of Ni@C

(0.002 s⁻¹), Ni₄Cu₁@C (0.019 s⁻¹), and Ni₄Cu₃@C (0.006 s⁻¹). Remarkably, the TOF of Ni₄Cu₂@C can be boosted to 0.169 s⁻¹ at an overpotential of 150 mV, exhibiting the largest enhancement (0.075 s⁻¹) among other Ni_xCu_y@C catalysts. The Ni₄Cu₂@C presents remarkable activity towards the HER because of the following reasons: (i) the hollow structure provides a large specific surface area with more exposed active sites, simultaneously enhancing the ion transfer. (ii) Improved electrical conductivity is induced by the introduction of Cu, which can create more free electrons.^{46,57} (iii) Moderate H adsorption free energy is another critical factor to determine the catalytic activity. After the optimal introduction of Cu, the binding strength of M–H_{ad} (M represents the surface active site) is weakened, facilitating the hydrogen adsorption and desorption processes.^{29,41,57,58} However, the HER activity will decrease if the Ni/Cu ratio is further increased to 4/3, because Cu is less active than Ni in the water splitting system, and excessive Cu on the surface would prevent active sites with high activity from being exposed, resulting in less competitive performance.^{24,59} To eliminate the contribution of the size, shape or morphology to electrocatalytic activity, the polarization curves have been normalized by ECSA (Fig. S5 and S6, ESI†).^{60,61}

As shown in Fig. S6b (ESI[†]), the Ni₄Cu₂@C still considerably outperforms other catalysts especially the original Ni, further confirming that the introduction of Cu plays a crucial role in improving the HER activity of Ni. Also, the EIS measurements reveal that the Ni_xCu_y@C electrocatalysts present small charge transfer resistance, suggesting fast electron transfer during the HER process (Fig. S7, ESI[†]). Especially after the introduction of Cu, R_{ct} decreases dramatically from 107.8 Ω (Ni@C) to 36.07 Ω (Ni₄Cu₂@C), indicating the promotion of charge transfer (Table S3, ESI[†]).

Moreover, the HER performance of the as-prepared samples in acidic medium was also investigated. Fig. 5d and e display the iR-corrected polarization curves of Ni_xCu_y@C samples and 20 wt% Pt/C in 0.5 M H₂SO₄, and the corresponding Tafel plots are employed to reveal the HER reaction mechanism. Obviously, the benchmark 20 wt% Pt/C still shows excellent performance toward the HER, which only needs the overpotential of 21 mV to achieve the current density of 10 mA cm⁻² and yields a small Tafel slope of 14 mV dec⁻¹. The Ni@C also shows relatively poor HER activity and a large Tafel slope. After the optimal amount of Cu incorporated into Ni, to drive the current density of 10 mA cm⁻², the applied overpotential for the Ni₄Cu₂@C is 91 mV, which is superior to other advanced HER electrocatalysts in 0.5 M H₂SO₄ (Fig. 5h and Table S4, ESI[†]). The Tafel slope value of Ni₄Cu₂@C is lower than that of the other Ni_xCu_y@C electrocatalysts, indicating much faster HER kinetics. The TOF values of Ni₄Cu₂@C are 0.057 and 0.137 s⁻¹ at the overpotential of 100 and 150 mV, which are the highest among other Ni_xCu_y@C samples, implying excellent intrinsic activity (Fig. 5f). Polarization curves normalized by ECSA further confirm the intrinsic activity of Ni_xCu_y@C

(Fig. S8 and S9, ESI[†]), excluding the structural effect. R_{ct} decreases dramatically from 195 Ω (Ni@C) to 28.64 Ω (Ni₄Cu₂@C), indicating the promotion of charge transfer after the optimal introduction of Cu (Fig. S10 and Table S5, ESI[†]).

Based on the above results and analyses, Ni₄Cu₂@C as a promising electrocatalyst reveals outstanding HER performance both in alkaline and acidic electrolytes. Compared to the previously reported electrocatalysts (Fig. 5i and Table S6, ESI[†]), the Ni₄Cu₂@C is highly active to deliver 10 mA cm⁻² current at 55 and 91 mV in 1 M KOH and 0.5 M H₂SO₄. Ni₄Cu₂@C presents almost 100% faradaic efficiency for the HER in both alkaline and acidic media *via* the water-gas displacing method, indicating that negligible by-products are formed during the electrolysis reaction (Fig. S11, ESI[†]). In addition, the stability test of the Ni₄Cu₂@C electrocatalyst was evaluated for an advanced electrocatalyst under various pH values. By chronopotentiometry analysis (Fig. S12, ESI[†]), the electrode stabilizes around the given potential (−0.055 V in 1 M KOH and −0.091 V in 0.5 M H₂SO₄) for about 20 h.

The Ni_xCu_y@C electrocatalysts are further investigated as OER electrocatalysts in 1 M KOH electrolyte. In contrast to Ni@C (407 mV), Ni₄Cu₁@C (372 mV), Ni₄Cu₃@C (429 mV) and other previously reported catalysts (Fig. 6a, b and Table S7, ESI[†]), the Ni₄Cu₂@C (283 mV) has a great performance at 10 mA cm⁻², even outperforming the commercial Ir/C catalyst (405 mV). Similarly, the Tafel slope of Ni₄Cu₂@C is superior to other Ni_xCu_y@C samples, indicating the fastest kinetics of mass and electron transfer (Fig. 6c). The TOF value of the Ni₄Cu₂@C is 0.055 s⁻¹ at an overpotential of 300 mV (Fig. 6d), which is much higher than those of Ni@C (0.017 s⁻¹), Ni₄Cu₁@C (0.025 s⁻¹), and Ni₄Cu₃@C (0.016 s⁻¹). And the

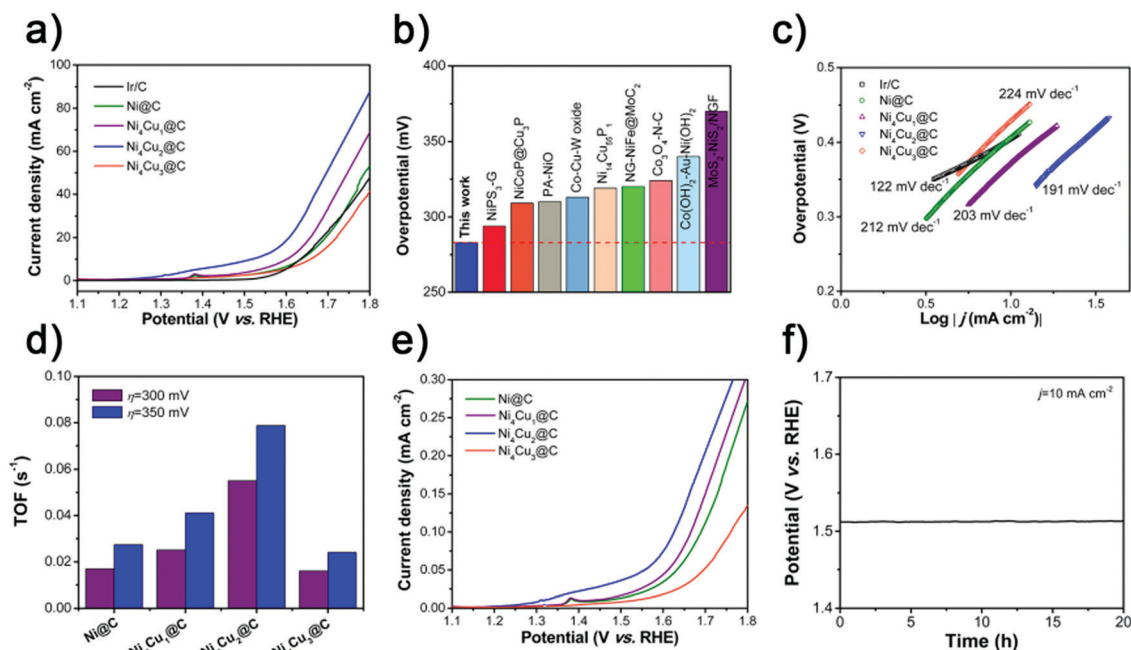


Fig. 6 (a) OER polarization curves, (b) comparison of the overpotential required at 10 mA cm⁻² with other recently reported OER electrocatalysts, (c) the corresponding Tafel plots, (d) TOFs, (e) OER polarization curves normalized by ECSA and (f) chronopotentiometry response of Ni₄Cu₂@C hollow spheres at the current density of 10 mA cm⁻².

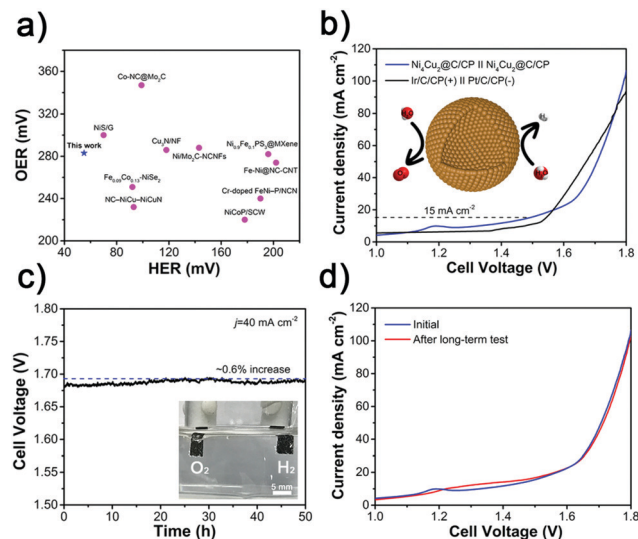
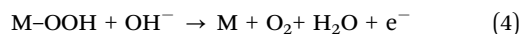
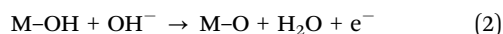
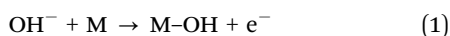


Fig. 7 (a) Comparison of the overpotential required at 10 mA cm^{-2} with other recently reported bifunctional electrocatalysts obtained in 1 M KOH, (b) polarization curves of overall water splitting in a two-electrode system, (c) chronopotentiometry response of $\text{Ni}_4\text{Cu}_2\text{@C}$ hollow spheres at the current density of 40 mA cm^{-2} (inset: the production of H_2 and O_2 bubbles on the surface of the electrode) and (d) polarization curves of $\text{Ni}_4\text{Cu}_2\text{@C}$ recorded before and after the 50 h chronopotentiometry test.

TOF value of $\text{Ni}_4\text{Cu}_2\text{@C}$ can be further boosted to 0.079 s^{-1} at an overpotential of 350 mV. These results further suggest that the $\text{Ni}_4\text{Cu}_2\text{@C}$ possesses excellent catalytic performance toward the OER. The overall OER process includes four elementary steps as follows:



The formation from M-O to M-OOH intermediates (step 3) is regarded as the rate-limiting step. The optimal Ni/Cu ratio can endow $\text{Ni}_x\text{Cu}_y\text{@C}$ with better electrical conductivity and generation of more active M-O species during the OER.^{62–64} Therefore, $\text{Ni}_4\text{Cu}_2\text{@C}$ presents excellent catalytic performance toward the OER rather than other $\text{Ni}_x\text{Cu}_y\text{@C}$ catalysts. By eliminating the effect of specific nanostructures, the polarization curves normalized by ECSA (Fig. 6e and Fig. S13, S14, ESI†) also demonstrate the highest activity of $\text{Ni}_4\text{Cu}_2\text{@C}$. The measured EIS also confirms the effect of Cu introduction on the charge-transfer resistance decreasing from 21.04Ω for Ni@C to 7.78Ω for $\text{Ni}_4\text{Cu}_2\text{@C}$ (Fig. S15 and Table S8, ESI†). The Faradaic efficiency of $\text{Ni}_4\text{Cu}_2\text{@C}$ is measured to be about 99.0% for 60 min electrolysis, reflecting high OER efficiency (Fig. S16, ESI†). Besides the high activity, excellent stability of the electrocatalysts toward the OER is also critical. Under the given potential (1.513 V) in 1 M KOH, the $\text{Ni}_4\text{Cu}_2\text{@C}$ can maintain the current density of 10 mA cm^{-2} for 20 h without any decline (Fig. 6f).

Encouraged by the highly catalytic activity of the $\text{Ni}_4\text{Cu}_2\text{@C}$ hollow spheres toward both the HER and OER in alkaline solution (Fig. 7a and Table S9, ESI†), we further utilized it as a bifunctional electrocatalyst for overall water electrolysis in a two-electrode system in 1 M KOH. Fig. 7b shows the polarization curves measured at a scan rate of 5 mV s^{-1} . The $\text{Ni}_4\text{Cu}_2\text{@C}$ affords a current density of 15 mA cm^{-2} at a cell voltage of as low as 1.49 V, comparable to commercial Ir/C-Pt/C (1.54 V). The high activity of $\text{Ni}_4\text{Cu}_2\text{@C}$ for overall water splitting manifests the compatible integration of the HER and the OER.^{65–67} The excellent performance also outperforms most of the recently reported bifunctional electrocatalysts (Table S10, ESI†). Moreover, the $\text{Ni}_4\text{Cu}_2\text{@C}$ exhibits excellent stability upon long-term testing under 40 mA cm^{-2} with only a very slight deactivation ($\sim 0.6\%$) over 50 h (Fig. 7c). Besides, after the long-term test, the polarization curves show no obvious shift (Fig. 7d). In order to inspect if there is any change in the morphology or composition of the $\text{Ni}_4\text{Cu}_2\text{@C}$ hollow spheres after the prolonged water splitting reaction, TEM, XRD, and XPS characterization studies were performed. On the cathode side, TEM images show that the morphology of $\text{Ni}_4\text{Cu}_2\text{@C}$ is well maintained (Fig. S17a and b, ESI†). HRTEM and XRD analyses also reveal no change in material composition (Fig. S17c and d, ESI†). The surface species of Ni^0 and Cu^0 can still be recognized after a long-term test (Fig. S17e and f, ESI†), indicating that Ni_4Cu_2 is stable in basic solutions during the HER.^{42,46,58} On the anode side, the nanostructure of $\text{Ni}_4\text{Cu}_2\text{@C}$ also remains intact (Fig. S18a and b, ESI†). However, by HRTEM analysis (Fig. S18c, ESI†), an amorphous layer is found on the surface of the hollow spheres, which is supposed to be the hydroxide species produced from alloys during electrolysis.^{62,68} Meanwhile, XRD patterns show no significant difference (Fig. S18d, ESI†), implying that the crystal structure is well-retained. XPS also displays that the surface metallic species of nickel and copper have disappeared and transformed into oxidized species (Fig. S16e and f, ESI†). Such *in situ* formed surface hydroxide species are considered to be the catalytic sites for the oxidation of OH^- to O_2 .^{69–71} Such excellent performance and durability render the $\text{Ni}_4\text{Cu}_2\text{@C}$ electrocatalyst a promising alternative to noble-metal electrocatalysts for water splitting in practical applications.

Conclusion

In summary, we have designed and synthesized a novel nickel-copper alloy with a hollow structure and tunable composition *via* a facile template-free solvothermal method. Benefiting from the large surface area and the introduction of Cu, the $\text{Ni}_x\text{Cu}_y\text{@C}$ hollow spheres with optimized molar ratios of Ni/Cu = 4/2 exhibit superior HER and OER performances, which can afford a current density of 10 mA cm^{-2} at small overpotentials of 55 and 283 mV in 1 M KOH, respectively. The $\text{Ni}_4\text{Cu}_2\text{@C}$ bifunctional catalyst electrode requires an applied voltage of only 1.49 V at a current density of 15 mA cm^{-2} to realize overall water splitting, outperforming most of the previously reported non-noble metal bifunctional electrocatalysts. This facile

template-free strategy can hopefully be extended to other functional materials with different compositions and nanostructures for applications in energy storage and conversion.

Conflicts of interest

There are no conflicts to declare.

Acknowledgements

We appreciate the financial support provided for this research by the National Key Research and Development Program of China (2017YFA0204600) and the National Natural Science Foundation of China (51721002 and 51673045).

References

- 1 M. K. Debe, Electrocatalyst approaches and challenges for automotive fuel cells, *Nature*, 2012, **486**, 43–51.
- 2 J. A. Turner, Sustainable Hydrogen Production, *Science*, 2004, **305**, 972–974.
- 3 X. Zou and Y. Zhang, Noble metal-free hydrogen evolution catalysts for water splitting, *Chem. Soc. Rev.*, 2015, **44**, 5148–5180.
- 4 Y. Wei, J. Wang, R. Yu, J. Wan and D. Wang, Constructing SrTiO₃-TiO₂ Heterogeneous Hollow Multi-shelled Structures for Enhanced Solar Water Splitting, *Angew. Chem., Int. Ed.*, 2019, **131**, 1436–1440.
- 5 P. Du and R. Eisenberg, Catalysts made of earth-abundant elements (Co, Ni, Fe) for water splitting: recent progress and future challenges, *Energy Environ. Sci.*, 2012, **5**, 6012.
- 6 M. Gong, W. Zhou, M. C. Tsai, J. Zhou, M. Guan, M. C. Lin, B. Zhang, Y. Hu, D. Y. Wang, J. Yang, S. J. Pennycook, B. J. Hwang and H. Dai, Nanoscale nickel oxide/nickel heterostructures for active hydrogen evolution electrocatalysis, *Nat. Commun.*, 2014, **5**, 4695.
- 7 Z. W. Seh, J. Kibsgaard, C. F. Dickens, I. Chorkendorff, J. K. Nørskov and T. F. Jaramillo, Combining theory and experiment in electrocatalysis: insights into materials design, *Science*, 2017, 355.
- 8 R. Ge, L. Li, J. Su, Y. Lin, Z. Tian and L. Chen, Ultrafine Defective RuO₂ Electrocatalyst Integrated on Carbon Cloth for Robust Water Oxidation in Acidic Media, *Adv. Energy Mater.*, 2019, **9**, 1901313.
- 9 J. Zhang, T. Wang, P. Liu, Z. Liao, S. Liu, X. Zhuang, M. Chen, E. Zschech and X. Feng, Efficient hydrogen production on MoNi₄ electrocatalysts with fast water dissociation kinetics, *Nat. Commun.*, 2017, **8**, 15437.
- 10 F. Hu, S. Zhu, S. Chen, Y. Li, L. Ma, T. Wu, Y. Zhang, C. Wang, C. Liu, X. Yang, L. Song, X. Yang and Y. Xiong, Amorphous Metallic NiFeP: A Conductive Bulk Material Achieving High Activity for Oxygen Evolution Reaction in Both Alkaline and Acidic Media, *Adv. Mater.*, 2017, 29.
- 11 L. Lin, M. Chen and L. Wu, Synthesis of Molybdenum-Tungsten Bimetallic Carbide Hollow Spheres as pH-Universal Electrocatalysts for Efficient Hydrogen Evolution Reaction., *Adv. Mater. Interfaces*, 2018, **5**, 1801302.
- 12 J. Lv, X. Yang, H.-Y. Zang, Y.-H. Wang and Y.-G. Li, Ultralong needle-like N-doped Co(OH)F on carbon fiber paper with abundant oxygen vacancies as an efficient oxygen evolution reaction catalyst, *Mater. Chem. Front.*, 2018, **2**, 2045–2053.
- 13 Z. Kang, H. Guo, J. Wu, X. Sun, Z. Zhang, Q. Liao, S. Zhang, H. Si, P. Wu, L. Wang and Y. Zhang, Engineering an Earth-Abundant Element-Based Bifunctional Electrocatalyst for Highly Efficient and Durable Overall Water Splitting, *Adv. Funct. Mater.*, 2019, **29**, 1807031.
- 14 P. Zhang, L. Li, D. Nordlund, H. Chen, L. Fan, B. Zhang, X. Sheng, Q. Daniel and L. Sun, Dendritic core-shell nickel-iron-copper metal/metal oxide electrode for efficient electrocatalytic water oxidation, *Nat. Commun.*, 2018, **9**, 381.
- 15 Z. Chen, Y. Ha, H. Jia, X. Yan, M. Chen, M. Liu and R. Wu, Oriented Transformation of Co-LDH into 2D/3D ZIF-67 to Achieve Co-N-C Hybrids for Efficient Overall Water Splitting, *Adv. Energy Mater.*, 2019, **9**, 1803918.
- 16 L. Lin, M. Chen and L. Wu, Hierarchical Iron-Doped Nickel Diselenide Hollow Spheres for Efficient Oxygen Evolution Electrocatalysis, *ACS Appl. Energy Mater.*, 2019, **2**, 4737–4744.
- 17 Q. Wang, Z. Liu, H. Zhao, H. Huang, H. Jiao and Y. Du, MOF-derived porous Ni₂P nanosheets as novel bifunctional electrocatalysts for the hydrogen and oxygen evolution reactions, *J. Mater. Chem. A*, 2018, **6**, 18720–18727.
- 18 X. Zhao, P. Pachfule, S. Li, J. R. J. Simke, J. Schmidt and A. Thomas, Bifunctional Electrocatalysts for Overall Water Splitting from an Iron/Nickel-Based Bimetallic Metal-Organic Framework/Dicyandiamide Composite, *Angew. Chem., Int. Ed.*, 2018, **57**, 8921–8926.
- 19 L. Li, C. Sun, B. Shang, Q. Li, J. Lei, N. Li and F. Pan, Tailoring the facets of Ni₃S₂ as a bifunctional electrocatalyst for high-performance overall water-splitting, *J. Mater. Chem. A*, 2019, **7**, 18003–18011.
- 20 Z. Li, W. Niu, L. Zhou and Y. Yang, Phosphorus and Aluminum Codoped Porous NiO Nanosheets as Highly Efficient Electrocatalysts for Overall Water Splitting, *ACS Energy Lett.*, 2018, **3**, 892–898.
- 21 P. Kuang, M. He, H. Zou, J. Yu and K. Fan, 0D/3D MoS₂-NiS₂/N-doped graphene foam composite for efficient overall water splitting, *Appl. Catal., B*, 2019, **254**, 15–25.
- 22 L. Lv, Z. Li, K.-H. Xue, Y. Ruan, X. Ao, H. Wan, X. Miao, B. Zhang, J. Jiang, C. Wang and K. Ostrikov, Tailoring the electrocatalytic activity of bimetallic nickel-iron diselenide hollow nanochains for water oxidation, *Nano Energy*, 2018, **47**, 275–284.
- 23 J. Nai, Y. Lu, L. Yu, X. Wang and X. W. D. Lou, Formation of Ni-Fe Mixed Diselenide Nanocages as a Superior Oxygen Evolution Electrocatalyst, *Adv. Mater.*, 2017, **29**, 1805541.
- 24 S.-Q. Liu, H.-R. Wen, G. Ying, Y.-W. Zhu, X.-Z. Fu, R. Sun and C.-P. Wong, Amorphous Ni(OH)₂ encounter with crystalline CuS in hollow spheres: a mesoporous nano-shelled heterostructure for hydrogen evolution electrocatalysis, *Nano Energy*, 2018, **44**, 7–14.
- 25 J. Lai, B. Huang, Y. Chao, X. Chen and S. Guo, Strongly Coupled Nickel-Cobalt Nitrides/Carbon Hybrid Nanocages

- with Pt-Like Activity for Hydrogen Evolution Catalysis, *Adv. Mater.*, 2019, **31**, 1805541.
- 26 K. Liu, C. Zhang, Y. Sun, G. Zhang, X. Shen, F. Zou, H. Zhang, Z. Wu, E. C. Wegener, C. J. Taubert, J. T. Miller, Z. Peng and Y. Zhu, High-Performance Transition Metal Phosphide Alloy Catalyst for Oxygen Evolution Reaction, *ACS Nano*, 2018, **12**, 158–167.
 - 27 Z. Chen, B. Zhao, Y.-C. He, H.-R. Wen, X.-Z. Fu, R. Sun and C.-P. Wong, NiCo₂O₄ nanoframes with a nanosheet surface as efficient electrocatalysts for the oxygen evolution reaction, *Mater. Chem. Front.*, 2018, **2**, 1155–1164.
 - 28 J. Wang, J. Wan and D. Wang, Hollow Multishelled Structures for Promising Applications: Understanding the Structure–Performance Correlation, *Acc. Chem. Res.*, 2019, **52**, 2169–2178.
 - 29 J. Y. Wang, Y. Cui and D. Wang, Design of Hollow Nanostructures for Energy Storage, Conversion and Production, *Adv. Mater.*, 2019, **31**, 1801993.
 - 30 J. Joo, T. Kim, J. Lee, S. I. Choi and K. Lee, Morphology-Controlled Metal Sulfides and Phosphides for Electrochemical Water Splitting, *Adv. Mater.*, 2019, **31**, 1806682.
 - 31 B. Y. Guan, L. Yu and X. W. D. Lou, Formation of Single-Holed Cobalt/N-Doped Carbon Hollow Particles with Enhanced Electrocatalytic Activity toward Oxygen Reduction Reaction in Alkaline Media, *Adv. Sci.*, 2017, **4**, 1700247.
 - 32 J. Wang, H. Tang, H. Wang, R. Yu and D. Wang, Multi-shelled hollow micro-/nanostructures: promising platforms for lithium-ion batteries, *Mater. Chem. Front.*, 2017, **1**, 414–430.
 - 33 M. Waqas, Y. Wei, D. Mao, J. Qi, Y. Yang, B. Wang and D. Wang, Multi-shelled TiO₂/Fe₂TiO₅ heterostructured hollow microspheres for enhanced solar water oxidation, *Nano Res.*, 2017, **10**, 3920–3928.
 - 34 J. Kibsgaard and T. F. Jaramillo, Molybdenum Phosphosulfide: An Active, Acid-Stable, Earth-Abundant Catalyst for the Hydrogen Evolution Reaction, *Angew. Chem., Int. Ed.*, 2014, **53**, 14433–14437.
 - 35 J. G. Speight, *Lange's Handbook of Chemistry*, McGraw-Hill Professional, New York, USA, 2005.
 - 36 T. Adschiri, K. Kanazawa and K. Arai, Rapid and Continuous Hydrothermal Crystallization of Metal Oxide Particles in Supercritical Water, *J. Am. Ceram. Soc.*, 1992, **75**, 1019.
 - 37 M. Kim, W.-S. Son, K. H. Ahn, D. S. Kim, H.-S. Lee and Y.-W. Lee., Hydrothermal synthesis of metal nanoparticles using glycerol as a reducing agent, *J. Supercrit. Fluids*, 2014, **90**, 53–59.
 - 38 B. Wierzbna and W. Skibiński, The interdiffusion in copper-nickel alloys, *J. Alloys Compd.*, 2016, **687**, 104–108.
 - 39 Y. Kawanami, M. Nakano, M. Kajihara and T. Mori, Growth rate of fine grains formed by diffusion induced recrystallization in Ni layer of Cu/Ni/Cu diffusion couples, *Mater. Trans.*, 1998, **39**, 218–224.
 - 40 K. K. Hong, J. B. Ryu, C. Y. Park and J. Y. Huh, Effect of Cross-Interaction between Ni and Cu on Growth Kinetics of Intermetallic Compounds in Ni/Sn/Cu Diffusion Couples during Aging, *J. Electron. Mater.*, 2007, **37**, 61–72.
 - 41 Y. Shen, Y. Zhou, D. Wang, X. Wu, J. Li and J. Xi, Nickel-Copper Alloy Encapsulated in Graphitic Carbon Shells as Electrocatalysts for Hydrogen Evolution Reaction, *Adv. Energy Mater.*, 2018, **8**, 1701759.
 - 42 B. Liu, H. Q. Peng, J. Cheng, K. Zhang, D. Chen, D. Shen, S. Wu, T. Jiao, X. Kong, Q. Gao, S. Bu, C. S. Lee and W. Zhang, Nitrogen-Doped Graphene-Encapsulated Nickel-Copper Alloy Nanoflower for Highly Efficient Electrochemical Hydrogen Evolution Reaction, *Small*, 2019, 1901545.
 - 43 H. Xu, Z. X. Shi, Y. X. Tong and G. R. Li, Porous Microrod Arrays Constructed by Carbon-Confined NiCo@NiCoO₂ Core@Shell Nanoparticles as Efficient Electrocatalysts for Oxygen Evolution, *Adv. Mater.*, 2018, **30**, 1705442.
 - 44 L. Yang, X. Zeng, D. Wang and D. Cao, Biomass-derived FeNi alloy and nitrogen-codoped porous carbons as highly efficient oxygen reduction and evolution bifunctional electrocatalysts for rechargeable Zn-air battery, *Energy Storage Mater.*, 2018, **12**, 277–283.
 - 45 H. Zhang, H. Jiang, Y. Hu, P. Saha and C. Li, Mo-Triggered amorphous Ni₃S₂ nanosheets as efficient and durable electrocatalysts for water splitting, *Mater. Chem. Front.*, 2018, **2**, 1462–1466.
 - 46 J. X. Feng, J. Q. Wu, Y. X. Tong and G. R. Li, Efficient Hydrogen Evolution on Cu Nanodots-Decorated Ni₃S₂ Nanotubes by Optimizing Atomic Hydrogen Adsorption and Desorption, *J. Am. Chem. Soc.*, 2018, **140**, 610–617.
 - 47 D. T. Tran, H. T. Le, T. L. Luyen Doan, N. H. Kim and J. H. Lee, Pt nanodots monolayer modified mesoporous Cu@Cu_xO nanowires for improved overall water splitting reactivity, *Nano Energy*, 2019, **59**, 216–228.
 - 48 Y. Xu, W. Tu, B. Zhang, S. Yin, Y. Huang, M. Kraft and R. Xu, Nickel Nanoparticles Encapsulated in Few-Layer Nitrogen-Doped Graphene Derived from Metal-Organic Frameworks as Efficient Bifunctional Electrocatalysts for Overall Water Splitting, *Adv. Mater.*, 2017, **29**, 1605957.
 - 49 A. Cuña, C. Reyes Plascencia, E. L. da Silva, J. Marcuzzo, S. Khan, N. Tancredi, M. R. Baldan and C. de Fraga Malfatti, Electrochemical and spectroelectrochemical analyses of hydrothermal carbon supported nickel electrocatalyst for ethanol electro-oxidation in alkaline medium, *Appl. Catal., B*, 2017, **202**, 95–103.
 - 50 P. He, X. Y. Yu and X. W. Lou, Carbon-Incorporated Nickel-Cobalt Mixed Metal Phosphide Nanoboxes with Enhanced Electrocatalytic Activity for Oxygen Evolution, *Angew. Chem., Int. Ed.*, 2017, **56**, 3897–3900.
 - 51 Y.-Y. Ma, C.-X. Wu, X.-J. Feng, H.-Q. Tan, L.-K. Yan, Y. Liu, Z.-H. Kang, E.-B. Wang and Y.-G. Li, Highly efficient hydrogen evolution from seawater by a low-cost and stable CoMoP@C electrocatalyst superior to Pt/C, *Energy Environ. Sci.*, 2017, **10**, 788–798.
 - 52 S. Jeoung, B. Seo, J. M. Hwang, S. H. Joo and H. R. Moon, Direct conversion of coordination compounds into Ni₂P nanoparticles entrapped in 3D mesoporous graphene for an efficient hydrogen evolution reaction, *Mater. Chem. Front.*, 2017, **1**, 973–978.
 - 53 G. Fu, Z. Cui, Y. Chen, Y. Li, Y. Tang and J. B. Goodenough, Ni₃Fe-N Doped Carbon Sheets as a Bifunctional Electrocatalyst for Air Cathodes, *Adv. Energy Mater.*, 2017, **7**, 1601172.

- 54 L. Yang and L. Zhang, N-enriched porous carbon encapsulated bimetallic phosphides with hierarchical structure derived from controlled electrodepositing multilayer ZIFs for electrochemical overall water splitting, *Appl. Catal., B*, 2019, **259**, 118053.
- 55 L. Yan, L. Cao, P. Dai, X. Gu, D. Liu, L. Li, Y. Wang and X. Zhao, Metal-Organic Frameworks Derived Nanotube of Nickel-Cobalt Bimetal Phosphides as Highly Efficient Electrocatalysts for Overall Water Splitting, *Adv. Funct. Mater.*, 2017, **27**, 1703455.
- 56 F. Lai, J. Feng, X. Ye, W. Zong, G. He, Y.-E. Miao, X. Han, X. Y. Ling, I. P. Parkin, B. Pan, Y. Sun and T. Liu, Energy level engineering in transition-metal doped spinel-structured nanosheets for efficient overall water splitting, *J. Mater. Chem. A*, 2019, **7**, 827–833.
- 57 J. Song, C. Zhu, B. Z. Xu, S. Fu, M. H. Engelhard, R. Ye, D. Du, S. P. Beckman and Y. Lin, Bimetallic Cobalt-Based Phosphide Zeolitic Imidazolate Framework: CoPxPhase-Dependent Electrical Conductivity and Hydrogen Atom Adsorption Energy for Efficient Overall Water Splitting, *Adv. Energy Mater.*, 2017, **7**, 1601555.
- 58 S. Chu, W. Chen, G. Chen, J. Huang, R. Zhang, C. Song, X. Wang, C. Li and K. Ostrikov, Holey Ni–Cu phosphide nanosheets as a highly efficient and stable electrocatalyst for hydrogen evolution, *Appl. Catal., B*, 2019, **243**, 537–545.
- 59 B. K. Kim, S.-K. Kim, S. K. Cho and J. J. Kim, Enhanced catalytic activity of electrodeposited Ni–Cu–P toward oxygen evolution reaction, *Appl. Catal., B*, 2018, **237**, 409–415.
- 60 Y. Y. Chen, Y. Zhang, W. J. Jiang, X. Zhang, Z. Dai, L. J. Wan and J. S. Hu, Pomegranate-like N,P-Doped Mo₂C@C Nanospheres as Highly Active Electrocatalysts for Alkaline Hydrogen Evolution, *ACS Nano*, 2016, **10**, 8851–8860.
- 61 S. Anantharaj, S. R. Ede, K. Karthick, S. Sam Sankar, K. Sangeetha, P. E. Karthik and S. Kundu, Precision and correctness in the evaluation of electrocatalytic water splitting: revisiting activity parameters with a critical assessment, *Energy Environ. Sci.*, 2018, **11**, 744–771.
- 62 C. Panda, P. W. Menezes, M. Zheng, S. Orthmann and M. Driess, In Situ Formation of Nanostructured Core–Shell Cu₃N–CuO to Promote Alkaline Water Electrolysis, *ACS Energy Lett.*, 2019, **4**, 747–754.
- 63 P. Li, X. Duan, Y. Kuang, Y. Li, G. Zhang, W. Liu and X. Sun, Tuning Electronic Structure of NiFe Layered Double Hydroxides with Vanadium Doping toward High Efficient Electrocatalytic Water Oxidation, *Adv. Energy Mater.*, 2018, **8**, 1703341.
- 64 Y. Lin, Y. Pan, S. Liu, K. Sun, Y. Cheng, M. Liu, Z. Wang, X. Li and J. Zhang, Construction of multi-dimensional core/shell Ni/NiCoP nano-heterojunction for efficient electrocatalytic water splitting, *Appl. Catal., B*, 2019, **259**, 118039.
- 65 Y. Guo, J. Tang, Z. Wang, Y.-M. Kang, Y. Bando and Y. Yamauchi, Elaborately assembled core–shell structured metal sulfides as a bifunctional catalyst for highly efficient electrochemical overall water splitting, *Nano Energy*, 2018, **47**, 494–502.
- 66 P. W. Menezes, C. Panda, S. Garai, C. Walter, A. Guet and M. Driess, Structurally Ordered Intermetallic Cobalt Stannide Nanocrystals for High-Performance Electrocatalytic Overall Water-Splitting, *Angew. Chem., Int. Ed.*, 2018, **57**, 15237–15242.
- 67 N. Yao, T. Tan, F. Yang, G. Cheng and W. Luo, Well-aligned metal–organic framework array-derived CoS₂ nanosheets toward robust electrochemical water splitting, *Mater. Chem. Front.*, 2018, **2**, 1732–1738.
- 68 V. R. Jothi, R. Bose, H. Rajan, C. Jung and S. C. Yi, Harvesting Electronic Waste for the Development of Highly Efficient Eco-Design Electrodes for Electrocatalytic Water Splitting, *Adv. Energy Mater.*, 2018, **8**, 1802615.
- 69 M. K. Bates, Q. Jia, H. Doan, W. Liang and S. Mukerjee, Charge-Transfer Effects in Ni–Fe and Ni–Fe–Co Mixed-Metal Oxides for the Alkaline Oxygen Evolution Reaction, *ACS Catal.*, 2015, **6**, 155–161.
- 70 T. Wang, G. Nam, Y. Jin, X. Wang, P. Ren, M. G. Kim, J. Liang, X. Wen, H. Jang, J. Han, Y. Huang, Q. Li and J. Cho, NiFe (Oxy) Hydroxides Derived from NiFe Disulfides as an Efficient Oxygen Evolution Catalyst for Rechargeable Zn–Air Batteries: The Effect of Surface S Residues, *Adv. Mater.*, 2018, **30**, 1800757.
- 71 Y. Feng, C. Xu, E. Hu, B. Xia, J. Ning, C. Zheng, Y. Zhong, Z. Zhang and Y. Hu, Construction of hierarchical FeP/Ni₂P hollow nanospindles for efficient oxygen evolution, *J. Mater. Chem. A*, 2018, **6**, 14103–14111.